Electronic Supplementary Materials

For https://doi.org/10.1631/jzus.A2300338

Numerical study on local failures of reinforced concrete slabs against underwater close-in explosions

Fei ZHOU[1], Hedong LI[2], Hao WU[1]✉

[1]*College of Civil Engineering, Tongji University, Shanghai 200092, China*
[2]*School of Civil Engineering and Architecture, Zhejiang Sci-Tech University, Hangzhou 310018, China*

✉ Hao WU, wuhaocivil@tongji.edu.cn

Section S1 Introduction of the proposed model for concrete

S1.1 Dynamic failure strength surface

Fig. S1 shows the failure strength surface, which contains tensile ($\sigma_1 \geq \sigma_2 \geq \sigma_3 \geq 0$), tensile-to-compressive ($\sigma_1 \geq 0 \geq \sigma_3$), and compressive ($0 \geq \sigma_1 \geq \sigma_2 \geq \sigma_3$) regions. Y represents the failure equivalent stress, and σ_i is the principal stress (i=1, 2, 3).

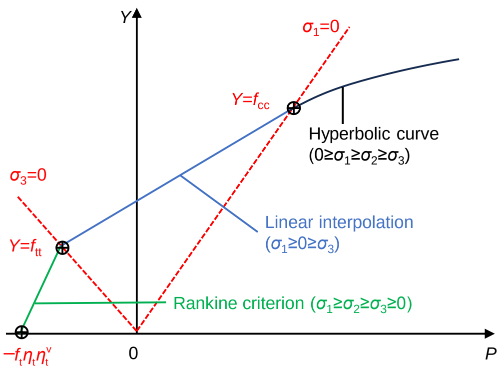

Fig. S1 Sketch diagram of failure strength surface (Zhou et al., 2023b)

In the compressive region, the proposed model adopts the 3D hyperbolic failure surface (Zhou et al., 2023b) given in Eq. (S1). It has an asymptote line of (P, Y)=($+\infty$, $S_{max}(0.25+0.75\eta_h)$) and interacts the σ_1=0 plane and P axis at (P, Y)=($2\cos\theta f_{cc}/3$, f_{cc}) and ($P_0\eta_s\eta_c^v$, 0), respectively, according to which it derives the expressions of a_1 and a_2. The Lode-angle θ, principal stress ratio α, and invariants of stress deviator tensor, i.e., J_2 and J_3, can capture the stress state. The damage functions η_h, η_s, and η_c^v describe the compressive strain hardening, compressive strain softening, and volumetric compaction damage on compressive strength, respectively. In Eq. (S1c), f_c^α is the biaxial compressive strength suggested by Kupfer and Gerstle (1973), where f_c is the uniaxial compressive strength and f_{bc} is the equal-biaxial compressive strength. Based on f_c^α, f_{cc} further considers the damage functions, i.e., η_h, η_s, and η_c^v, and the $\sqrt{1+\alpha^2}-\alpha$ term caused by transforming f_c^α from $\sigma_1-\sigma_3$ to $\sqrt{3J_2}$.

$$Y=\sqrt{3J_2}=f_{cc}+\frac{P-\frac{2}{3}\cos\theta f_{cc}}{a_1+a_2\left(P-P_0\eta_s\eta_c^v\right)}, \text{for } P>\frac{2}{3}\cos\theta f_{cc}, \tag{S1a}$$

$$a_1=\frac{2}{3}\cos\theta-\frac{P_0\eta_s\eta_c^v}{f_{cc}}, a_2=\frac{1}{S_{max}\left(0.25+0.75\eta_h\right)-f_{cc}}, \tag{S1b}$$

$$f_{cc}=f_c^{\alpha}\left(0.45+0.55\eta_h\right)\eta_s\eta_c^v\sqrt{1+\alpha^2-\alpha},\ f_c^{\alpha}=f_c\frac{1+\alpha\left(4\frac{f_{bc}}{f_c}-1\right)}{\left(1+\alpha\right)^2}, \tag{S1c}$$

$$\theta=\frac{1}{3}\text{acos}\left(\frac{3\sqrt{3}}{2}\frac{J_3}{J_2^{1.5}}\right),\quad \alpha=\frac{\sigma_1-\sigma_2}{\sigma_1-\sigma_3}=\frac{\cos\left(\frac{2\pi}{3}-\theta\right)-\cos\left(\frac{2\pi}{3}+\theta\right)}{\cos\theta-\cos\left(\frac{2\pi}{3}+\theta\right)}. \tag{S1d}$$

In the tensile region, the proposed model uses the Rankine criterion (Rankine, 1908), i.e., Eq. (S2), which interacts with the σ_3=0 plane and P axis at (P, Y)=(2cos(2π/3+θ)f_{tt}/3, f_{tt}) and ($-f_t\eta_t\eta_t^v$, 0), respectively. The damage functions η_t and η_t^v describe the tensile strain softening and volumetric compaction damage, respectively, on the tensile strength. f_{tt} is the $\sqrt{3J_2}$ of the uniaxial tensile strength f_t with damage functions, i.e., $f_{tt}=f_t\eta_t\eta_t^v\sqrt{1+\alpha^2-\alpha}$.

$$Y=\sqrt{3J_2}=\frac{3\left(P+f_t\eta_t\eta_t^v\right)}{2\cos\theta}, \text{for}\quad -f_t\eta_t\eta_t^v\le P\le\frac{2}{3}\cos\left(\frac{2}{3}\pi+\theta\right)f_{tt}. \tag{S2}$$

In the tensile-to-compressive region, the failure strength surface Eq. (S3) is obtained by interpolating linearly between the boundaries of the tensile and compressive regions.

$$Y=\sqrt{3J_2}=\ f_{tt}+\frac{P-\frac{2}{3}\cos\left(\frac{2}{3}\pi+\theta\right)f_{tt}}{\frac{2}{3}\cos\theta f_{cc}-\frac{2}{3}\cos\left(\frac{2}{3}\pi+\theta\right)f_{tt}}\left(f_{cc}-f_{tt}\right), \text{for}\ \frac{2}{3}\cos\left(\frac{2}{3}\pi+\theta\right)f_{tt}<P\le\frac{2}{3}\cos\theta f_{cc}. \tag{S3}$$

Under dynamic loadings, the proposed model uses the radial enhancement approach presented in Eq. (S4) to describe the strain rate effect. The parameters Y_{DIF} and P_{DIF} denote the Y and P containing the strain rate effect, i.e., the dynamic increase factor (DIF).

$$Y_{DIF}\left(P_{DIF}\right)=\text{DIF}\cdot Y\left(P\right),\ \text{where}\ P=\frac{P_{DIF}}{\text{DIF}}. \tag{S4}$$

S1.2 Damage functions

The proposed model considers the damage from shear deformation, i.e., η_h, η_s, and η_t, and volumetric compaction, i.e., η_c^v and η_t^v , and defines the compressive, tensile, volumetric compressive, volumetric tensile, and total damage as D_c=1−η_s, D_t=1−η_t, D_{vc}=1−η_c^v , D_{vt}=1−η_t^v , and D=1−(1−D_c)(1−D_t)(1−D_{vc}) (1−D_{vt}), respectively. Eq. (S5) gives the damage functions to describe the compressive strain hardening η_h, compressive strain softening η_s (Sargin, 1971), and tensile strain softening η_t (Hordijk, 1991). Parameter A affects the compressive strain softening slop, η_s accumulates once η_h reaches 1, and ε_{frac}=0.007 is the fracture strain (Xu and Wen, 2016).

$$\eta_h=1-\left[1-\min\left(\lambda_h,1\right)^{0.8}\right]^{1.8} \text{ and } \eta_s=\max\left[\frac{1+\lambda_s+\left(A-1\right)\left(1+\lambda_s\right)^2}{A\left(1+\lambda_s\right)^2-\lambda_s},\frac{f_t}{f_c}\right]. \tag{S5a}$$

$$\eta_t=\left[1+27\left(\frac{\lambda_t}{\varepsilon_{frac}}\right)^3\right]\exp\left(-6.93\frac{\lambda_t}{\varepsilon_{frac}}\right)-28\frac{\lambda_t}{\varepsilon_{frac}}\exp\left(-6.93\right). \tag{S5b}$$

Eq. (S6) presents the equivalent plastic strain λ, i.e., λ_h, λ_s, and λ_t, to accumulate these shear deformation damage functions, where $\Delta\varepsilon_e^p$ is the effective plastic strain $\sqrt{2\Delta\varepsilon_{ij}^p\Delta\varepsilon_{ij}^p/3}$, $\Delta\varepsilon_1^p$ denotes the maximum principal plastic strain, and d_1^s, d_1^h, and d_2 are damage parameters. It uses a stress state-related parameter β to consider the continued transition from compression to tension. As shown in Eq. (S7), m is the value of β when P=0, and β_c and β_t are stress state-related interpolation coefficients.

$$\lambda_h = \sum \frac{\beta\Delta\varepsilon_e^p}{\mathrm{DIF}\cdot d_1^h\left[1+\frac{\max(P,0)}{f_t}\right]^{d_2}}, \lambda_s = \sum \frac{\beta\Delta\varepsilon_e^p}{\mathrm{DIF}\cdot d_1^s\left[1+\frac{\max(P,0)}{f_t}\right]^{d_2}}, \lambda_t = \sum(1-\beta)\Delta\varepsilon_1^p. \quad \text{(S6)}$$

$\beta = m - m\beta_t + (1-m)\beta_c$, where

$$\beta_t = \max\left\{0, \min\left(1, \frac{\frac{1.5P}{\sqrt{3J_2}}}{\cos\left(\theta+\frac{2\pi}{3}\right)}\right)\right\}, \beta_c = \max\left\{0, \min\left(1, \frac{\frac{1.5P}{\sqrt{3J_2}}}{\cos\theta}\right)\right\}. \quad \text{(S7)}$$

Eq. (S8) presents the volumetric damage functions, where f_d reflects the contribution of stress state, $P_{\mathrm{DIF}}^{\max}$ is the maximum pressure during calculation, and the superscripts 'old' and 'new' denote parameters in the current and previous time steps, respectively.

$$\eta_c^v = 1-\sum f_d\left(r_c^{old}-r_c^{new}\right), \eta_t^v = 1-\sum f_d\left(r_t^{old}-r_t^{new}\right), \quad \text{(S8a)}$$

$$r_c = \max\left(1, \frac{P_{\mathrm{DIF}}^{\max}}{f_c}\right)^{\frac{-0.007 f_c}{\mathrm{MPa}}}, r_t = \max\left(1, \frac{P_{\mathrm{DIF}}^{\max}}{f_c}\right)^{\frac{-0.3 f_t}{\mathrm{MPa}}}, f_d = \max\left[0, 1-\frac{\cos\theta}{\frac{1.5P}{\sqrt{3J_2}}}\right]. \quad \text{(S8b)}$$

S1.3 EOS and plastic flow rule

The proposed model uses the tabulated EOS (*EOS_8 in LS-DYNA) to account for the nonlinear relation between volumetric strain μ and hydrostatic pressure P_{DIF}, as presented in Eq. (S9) and Fig. S2. The input parameters (μ_n, P_n) define the plastic compaction path and $K_{u,n}$ determines the corresponding elastic unloading/reloading path.

$$\begin{cases} P_{\mathrm{DIF}} = \dfrac{\mu-\mu_n}{\mu_{n+1}-\mu_n}\left(P_{n+1}-P_n\right), \\ K_u = \dfrac{\mu-\mu_n}{\mu_{n+1}-\mu_n}\left(K_{u,n+1}-K_{u,n}\right), \end{cases} \text{for } \mu_n < \mu \le \mu_{n+1}. \quad \text{(S9)}$$

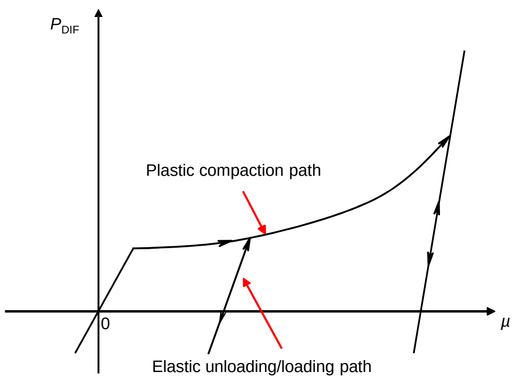

Fig. S2 Sketch diagram of the equation of state (Zhou et al., 2023b)

The proposed model uses an independent plastic potential function to describe the shear dilation of concrete, which is the 3D hyperbolic failure surface at the initial state (η_h=0 and $\eta_s = \eta_c^v$ =1). Besides, it is implemented in LS-DYNA (Version R5.1.1) as a user-defined material model.

Section S2 Parameters of the proposed model for dry concrete

Table S1 presents the parameters of the proposed model for dry concrete.

Table S1 Parameters of the proposed model for dry concrete (*w*=0)

Basic		f_c, f_t=0.3$f_c^{0.67}$, ρ, E=4730$f_c^{0.5}$, v=0.2, G=E/2(1+v), K=E/3(1−2v)									
Strength surface		S_{max}=2600 MPa, P_0=−0.33f_c, f_{bc}=1.25f_c									
Strain rate effect		W_x=1.75, S=1.1, F_m=10, W_y=5.5, w=0									
Damage function		m=0, A=1.05, d_2=1, d_1^h=0.0001(5−f_c/20 MPa), d_1^s=0.08(f_c/MPa)$^{-1.33}$, ε_{frac}=0.007									
	μ_1–μ_{10}	0	0.0015	0.0043	0.0101	0.0305	0.0513	0.0726	0.0943	0.1740	0.2080
EOS	P_1–P_{10}	0	μ_2K	$2\mu_2K$	$3.5\mu_2K$	$8\mu_2K$	$14\mu_2K$	$20\mu_2K$	$28\mu_2K$	$127\mu_2K$	$195\mu_2K$
	$K_{u,1}$–$K_{u,10}$	K	K	1.014K	1.065K	1.267K	1.47K	1.672K	1.825K	4.107K	5K

Section S3 Sketch of the single-element test

Fig. S3 presents a sketch of the single-element test, which brings uniaxial compressive or tensile displacement to bear on a cube element with an edge length of 10 mm to simulate the uniaxial compression or tension test. It further applies the confining pressures on the side surfaces of the cube element in the triaxial compression test.

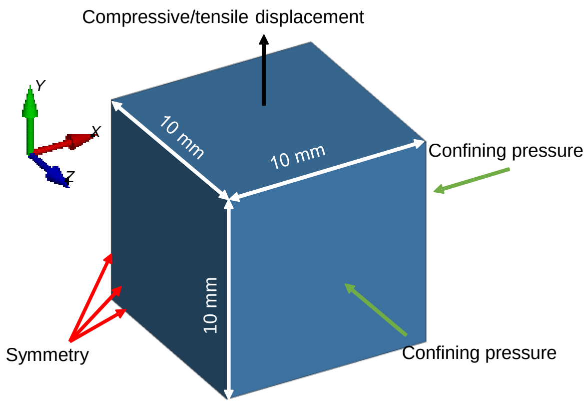

Fig. S3 A sketch of the single-element test

Section S4 Material models of steel, explosive, air and water

S4.1 Steel

The *MAT_PLASTIC_KINEMATIC model that can consider the isotropic/kinematic hardening effect was used to simulate the steel reinforcement or frame. It describes the strain rate effect using the Cowper-Symonds model, as given in Eq. (S10), where C and P are the strain rate parameters, and $\dot{\varepsilon}$ is the strain rate. Table S2 lists the parameters of the steel (Zhou et al., 2023a).

$$\mathrm{DIF} = 1 + \left(\frac{\dot{\varepsilon}}{C}\right)^{\frac{1}{P}}. \tag{S10}$$

Table S2 Plastic kinematic model parameters of the steel (Zhou et al., 2023a)

ρ (kg/m^3)	E (GPa)	v	Yield strength (MPa)	E_t (GPa)	C (s^{-1})	P	Failure strain
7800	210	0.3	400/235	2	40	5	0.14

S4.2 Explosives

The high energy combustion (CJ) model, i.e., the *MAT_HIGH_EXPLOSIVE_BURN, combined with the Jones-Wilkens-lee (JWL) EOS was adopted to simulate the detonation process of the explosive. The pressure in the explosive element was determined by Eq. (S11), where F is the burn fraction, p_{EOS} is the shock wave pressure obtained from the EOS, V is the relative volume, E is the initial internal energy in unit volume, A, B, R_1, R_2, and ω are the EOS coefficients. Table S3 lists the parameters of the TNT (Xu et al., 2022) and emulsion explosives (Yang et al., 2023). The time and location of the detonation point are defined by *INITIAL_DETONATION.

$$p = F p_{\text{EOS}}\left(V, E\right), \tag{S11a}$$

$$p_{\text{EOS}} = A\left(1-\frac{\omega}{R_1 V}\right)e^{-R_1 V} + B\left(1-\frac{\omega}{R_2 V}\right)e^{-R_2 V} + \frac{\omega E}{V}. \tag{S11b}$$

Table S3 CJ model and JWL EOS parameters for the explosives

Explosives	ρ (kg/m^3)	D (m/s)	P_{cj} (GPa)	A (GPa)	B (GPa)	R_1	R_2	ω	E_0 (J/m^3)
TNT	1630	6930	21.0	373.8	3.747	4.15	0.9	0.35	6.0×10^9
Emulsion	1150	5500	7.4	214.4	0.182	4.20	0.9	0.15	4.2×10^9

S4.3 Air

The air was simulated as a non-viscous ideal gas with no shear strength. The model adopts *MAT_NULL to describe the basic property of air, i.e., the density. The air pressure is accounted for by the *EOS_LINEAR_POLYNOMIAL given in Eq. (S12), where E is the initial internal energy per unit volume, μ is the volumetric strain, and C_0–C_6 are the EOS coefficients. Table S4 presents the material parameters of the air (Xu et al., 2022).

$$P = C_0 + C_1\mu + C_2\mu^2 + C_3\mu^3 + \left(C_4 + C_5\mu + C_6\mu^2\right)E. \tag{S12}$$

Table S4 *MAT_NULL and *EOS_LINEAR_POLYNOMIAL parameters for the air (Xu et al., 2022)

ρ (kg/m^3)	E (MPa)	Pressure cutoff	C_0	C_1	C_2	C_3	C_4	C_5	C_6
1.29	0.25	0	0	0	0	0	0.4	0.4	0.6

S4.4 Water

*MAT_NULL and *EOS_GRUNEISEN were adopted to simulate the water. The pressure in water is determined by Eq. (S13a) in the compressed state and Eq. (S13b) in the expanded state, which is related to the function of the shock velocity-particle velocity, i.e., $v_s(v_p)$. The parameter C is the intercept of the $v_s(v_p)$ function, S_1, S_2, and S_3 are the coefficients of the slope of the $v_s(v_p)$ function, γ_0 is the Gruneisen gamma, a is the volume correction to γ_0, and E is the initial internal energy per unit volume. The parameters of the water are listed in Table S5 (Song et al., 2017).

$$P = \frac{\rho_0 C^2 \mu\left[1+\left(1-\frac{\gamma_0}{2}\right)\mu - \frac{a\mu^2}{2}\right]}{\left[1-\left(S_1-1\right)\mu - \frac{S_2\mu^2}{\left(1+\mu\right)} - \frac{S_3\mu^3}{\left(1+\mu\right)^2}\right]^2} + \left(\gamma_0 + a\mu\right)E, \tag{S13a}$$

$$P = \rho_0 C^2 \mu + \left(\gamma_0 + a\mu\right)E. \tag{S13b}$$

Table S5 *MAT_NULL and *EOS_GRUNEISEN parameters for the water (Song et al., 2017)

ρ_0 (kg/m^3)	E (MPa)	S_1	S_2	S_3	γ_0	a	C (m/s)
1020	0	1.92	−0.096	0	0.25	0	1650

Section S5 Effect of different damage (D_c, D_t, D_{vc}, D_{vt}) on the failure patterns

Corresponding to Section 3.1, Fig. S4 presents the predicted compressive (D_c), tensile (D_t), volumetric compressive (D_{vc}), volumetric tensile (D_{vt}), and total (D) damage of the T1 target. The compressive and tensile damage caused by the shear deformation dominates the failure of the T1 target under the UWCI explosion. Comparatively, the damage caused by volumetric compaction had a negligible effect since the peak pressure of the shock wave decreased rapidly with increasing distance, and the stress state of the concrete material did not lie in hydrostatic compression. Besides, the tensile damage was much more severe than the compressive damage, and the tensile damage pattern was almost the same as the total damage pattern. Therefore, the failure of the RC orifice under a UWCI explosion is affected mainly by the mechanical properties of the concrete material in the low-pressure range, especially the tensile property.

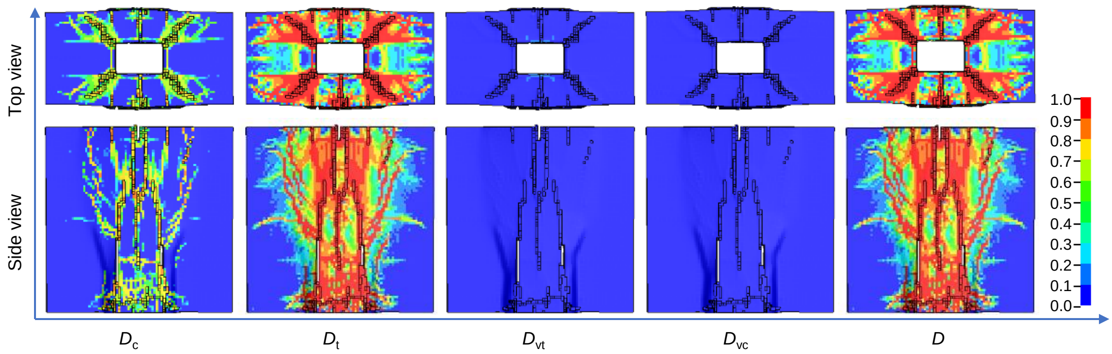

Fig. S4 Predicted damage variables of the T1 target under a UWCI explosion

Corresponding to Section 3.2, Fig. S5 presents the predicted D_c, D_t, D_{vc}, D_{vt}, and D in the 10-g TNT test scenario. The volumetric damage (D_{vc}, D_{vt}) was minor and concentrated near the center of the front surface. The reason is that only the concrete near the explosive suffered from the significant shock wave pressure. The rear part of the saturated concrete slab experienced a smaller shock wave pressure or did not lie in the hydrostatic compaction state. In contrast, the shear damage (D_c, D_t) was prominent and had a larger extent of distribution near the rear surface since the shear deformation was larger than the volumetric compaction deformation. The tensile damage D_t had a larger distribution area and greater extent than the D_c, because the concrete becomes fragile as the pressure decreases. Combined with Figs. S4 and S5, we conclude that the failure of concrete structures under a UWCI explosion is inherently caused by the tensile damage, even for those materials adjacent to the detonation point.

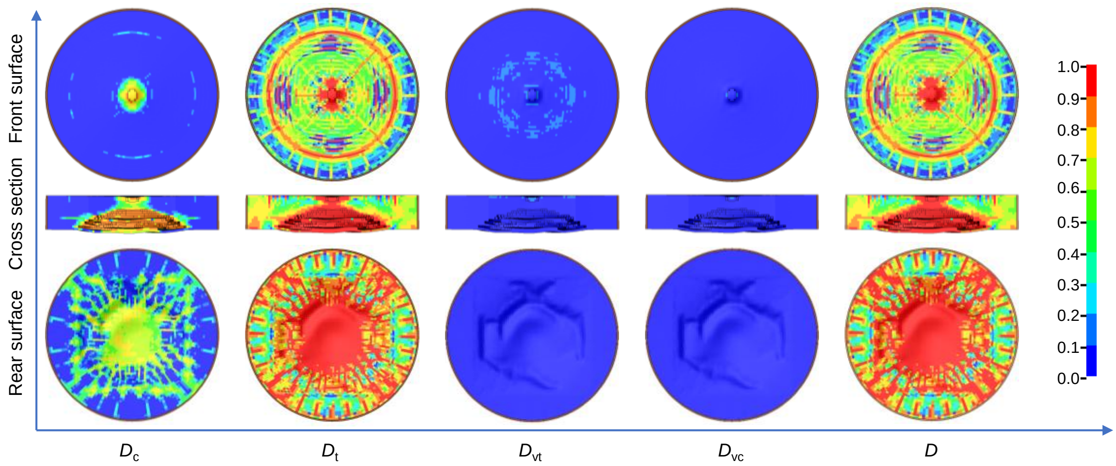

Fig. S5 Predicted damage variables of the saturated concrete slab in the 10-g TNT test scenario

Section S6 Difference in the shock wave propagation processes between water/air-back scenarios

Corresponding to Section 4.2.4, Fig. S6 presents the shock wave propagation processes. The shock wave reaches the front and rear RC slab surfaces at nearly 0.04 and 0.11 ms, respectively. There is almost no difference in the propagation of the shock wave before it reaches the rear surface. As the shock wave propagates further into the distal side, the shock wave transmitted in the water is significantly larger than that in the air due to the difference in wave impedance between water and air. Specifically, the peak shock wave at the point I' in the water is about 4000 times that in the air, i.e., 118 vs. 0.029 MPa. Compared to the air, the water in the distal surface could transmit a larger shock wave, reduce the reflected tensile shock wave in the RC slab, and thereby alleviate the local and structural failure of the RC slab.

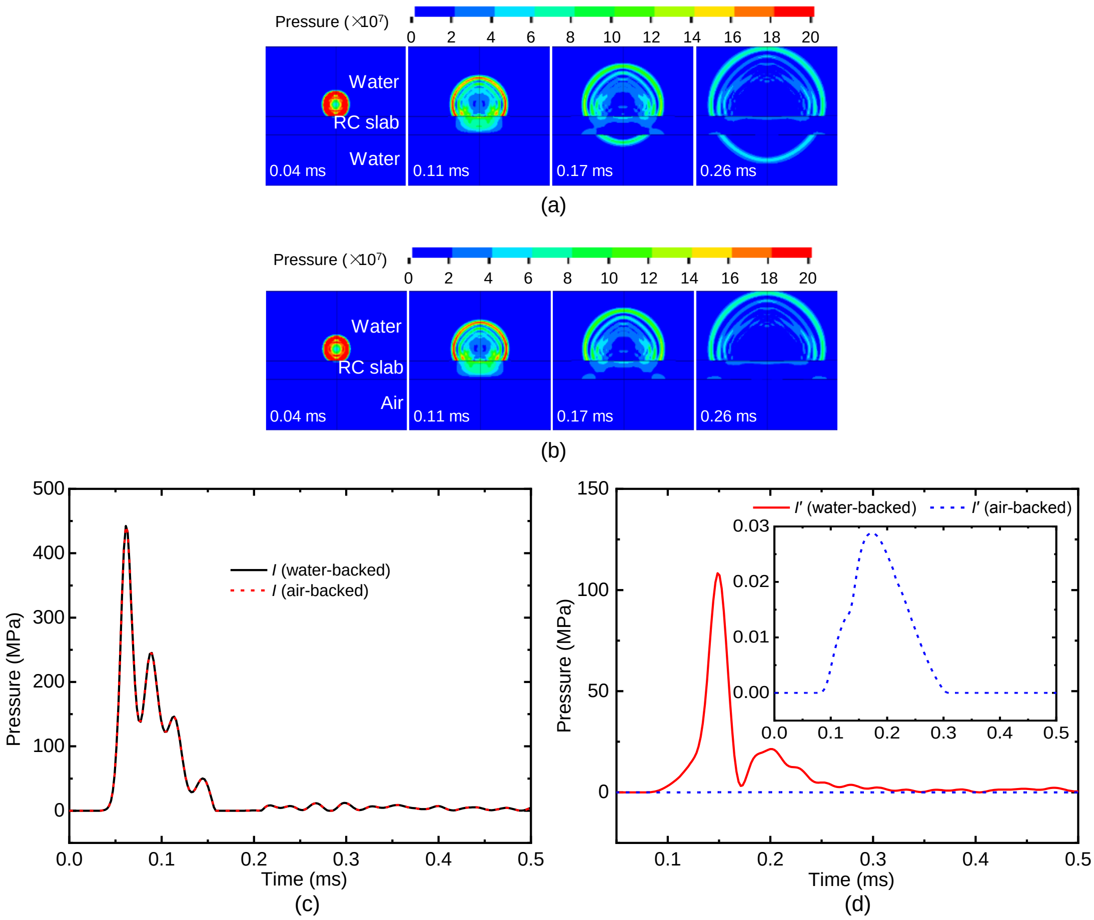

Fig. S6 Effect of water/air-back conditions on the shock wave: (a) water-back scenario; (b) air-back scenario; (c) incident surface; (d) distal surface

References

Hordijk DA, 1991. Local Approach to Fatigue of Concrete. PhD Thesis, Delft University of Technology, Delft, The Netherlands.

Kupfer HB, Gerstle KH, 1973. Behavior of concrete under biaxial stresses. *Journal of the Engineering Mechanics Division*, 99(4):853-866. https://doi.org/10.1061/JMCEA3.0001789

Rankine WJM, 1858. A Manual of Applied Mechanics. C. Griffin and Co, London, UK. https://babel.hathitrust.org/cgi/pt?id=uc1.b3141142&seq=5

Sargin M, 1971. Stress-strain relationships for concrete and the analysis of structural concrete sections. Solid Mechanics Division, University of Waterloo: Waterloo, ON, Canada, Volume 4, p.167.

Song G, Chen ZY, Long Y, et al., 2017. Experimental and numerical investigation of the centrifugal model for underwater explosion shock wave and bubble pulsation. *Ocean Engineering*, 142:523-531. https://doi.org/10.1016/j.oceaneng.2017.04.035

Xu H, Wen HM, 2016. A computational constitutive model for concrete subjected to dynamic loadings. *International Journal of Impact Engineering*, 91:116-125. https://doi.org/10.1016/j.ijimpeng.2016.01.003

Xu JP, Wu H, Ma LL, et al., 2022. Residual axial capacity of seismically designed RC bridge pier after near-range explosion of vehicle bombs. *Engineering Structures*, 265:114487. https://doi.org/10.1016/j.engstruct.2022.114487
Yang GD, Fan Y, Wang GH, et al., 2023. Experimental and numerical investigation on dynamic behavior of RC orifice targets subjected to underwater explosions. *Engineering Structures*, 279:115541. https://doi.org/10.1016/j.engstruct.2022.115541
Zhou F, Cheng YH, Peng Q, et al., 2023a. Influence of steel reinforcement on the performance of an RC structure subjected to a high-velocity large-caliber projectile. *Structures*, 54:716-731. https://doi.org/10.1016/j.istruc.2023.05.096
Zhou F, Wu H, Cheng YH, 2023b. Perforation studies of concrete panel under high velocity projectile impact based on an improved dynamic constitutive model. *Defence Technology*, 27:64-82. https://doi.org/10.1016/j.dt.2022.09.004